Deformation of 4H-SiC: The role of dopants ⊘

Xiaoshuang Liu; Junran Zhang; Binjie Xu; Yunhao Lu; Yiqiang Zhang; Rong Wang ✉ iD ; Deren Yang iD ; Xiaodong Pi ✉ iD

Check for updates

View Online

Export Citation

Deformation of 4H-SiC: The role of dopants

View Online   Export Citation   CrossMark

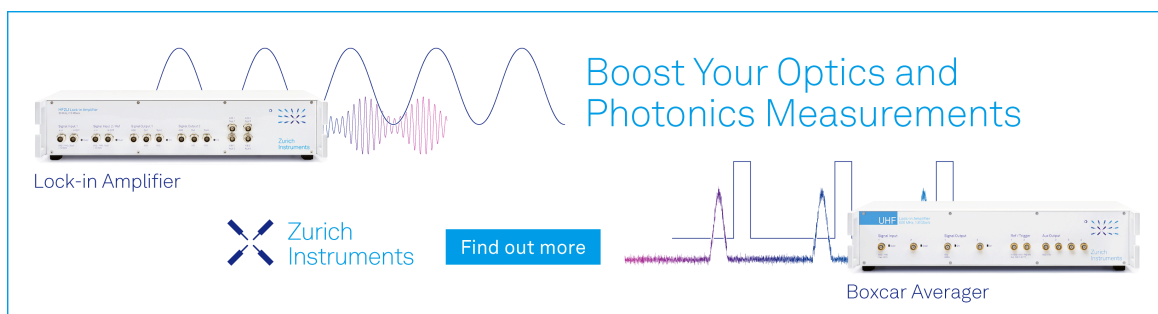Xiaoshuang Liu,[1,2] Junran Zhang,[1,2] Binjie Xu,[1,2] Yunhao Lu,[3] Yiqiang Zhang,[4] Rong Wang,[2,a] (iD) Deren Yang,[1,2] (iD)
and Xiaodong Pi[1,2,a] (iD)

AFFILIATIONS

[1]State Key Laboratory of Silicon Materials and School of Materials Science and Engineering, Zhejiang University, Hangzhou 310027,
 China
[2]Hangzhou Innovation Center, Zhejiang University, Hangzhou 311200, China
[3]Zhejiang Province Key Laboratory of Quantum Technology and Device & Department of Physics, Zhejiang University,
 Hangzhou 310027, China
[4]School of Materials Science and Engineering & Henan Institute of Advanced Technology, Zhengzhou University, Zhengzhou,
 Henan 450001, China

[a]Authors to whom correspondence should be addressed: rong_wang@zju.edu.cn and xdpi@zju.edu.cn

ABSTRACT

The role of dopants on deformation and mechanical properties of 4H silicon carbide (4H-SiC) is proposed by using nanoindentation. It is found that the hardness, elastic modulus, and fracture toughness of 4H-SiC substrate wafers all decrease on the order of vanadium (V) doping, undoping, and nitrogen (N) doping. For all three types of 4H-SiC, basal plane dislocations (BPDs), threading edge dislocations, and cracks are formed during the nanoindentation. Polymorph transitions from 4H-SiC to amorphous SiC and 3C-SiC are found as the penetration depth of the indent increases from the subsurface to the deeper region. N doping is found to weaken the bond strength of 4H-SiC, which enhances the glide and piling up of BPDs in nanoindented N-doped 4H-SiC. In contrast, V doping effectively hinders the glide of BPDs, which accumulates a high-stress field and facilitates the polymorph transition from 4H-SiC to 3C-SiC and amorphous SiC. The insight on the effects of dopants on the deformation and mechanical properties of 4H-SiC may help the design of the processing of differently doped 4H-SiC substrate wafers.

Published under an exclusive license by AIP Publishing. https://doi.org/10.1063/5.0083882

As a leading wide-bandgap semiconductor, 4H silicon carbide (4H-SiC) is attracting great attention due to the explosive demand of electrical vehicles, 5G communications, and renewable-energy systems.[1–4] 4H-SiC single crystals are usually grown by the physical vapor transport (PVT) approach. After the growth, 4H-SiC is processed to form substrate wafers by using wire cutting, lapping, and chemical mechanical polishing (CMP). Despite the progress of the substrate-wafer processing of 4H-SiC over years, high-density processing damages remain in 4H-SiC substrate wafers.[5,6] In addition, the processing of 4H-SiC substrate wafers suffer from the issues of low yield, low efficiency, and limited control of flatness given the high hardness and brittleness of 4H-SiC.[7] Clearly, the improvement of the processing capacity and, thus, quality of 4H-SiC substrate wafers demands thorough understanding of the deformation mechanism and, thus, mechanical properties of 4H-SiC.

Nanoindentation has been demonstrated as a powerful technique for investigation of mechanical properties of 4H-SiC.[8] Nawaz *et al.* measured the nanoscale elastic-plastic response of 4H-SiC through the

nanoindentation experiment and revealed that the hardness and elastic modulus of 4H-SiC are 36 and 413 GPa, respectively.[9] It has been theoretically shown that nanoindentation generates defects such as basal plane dislocations (BPDs) of 4H-SiC and gives rise to polymorph transition.[10] Meanwhile, dopants have been found to interplay with defects, changing the behavior of defects in semiconductors.[11,12] For commercially available 4H-SiC substrate wafers, vanadium (V) and nitrogen (N) are the most common dopants, which lead to semi-insulting and *n*-type 4H-SiC, respectively.[13] The concentrations of V and N are typically on the order of magnitude of 10^{17} and $10^{19}\,cm^{-3}$, respectively.[14–16] It is reasonable to expect that the high-concentration dopants may interplay with processing-induced defects and affect the deformation of 4H-SiC during the processing of 4H-SiC substrate wafers. However, the effect of dopants on the deformation mechanism and, thus, the mechanical properties of 4H-SiC is still ambiguous, which hinders the optimization of processing capacity of 4H-SiC substrate wafers.

In this work, nanoindentation is employed to investigate the deformation of undoped, V-doped, and N-doped 4H-SiC substrate

07 April 2024 10:11:03

wafers. Undoped 4H-SiC is usually referred to as high-purity semi-insulating (HPSI) 4H-SiC, which is grown without any intentional doping. We find that the hardness, elastic modulus, and fracture toughness of 4H-SiC all decrease on the order of V doping, undoping, and N doping. For all the three types of 4H-SiC, BPDs, threading edge dislocations (TEDs) and cracks are formed during the nanoindentation. Polymorph transitions from 4H-SiC to 3C-SiC and amorphous SiC are found as the penetration depth of the indent increases from the subsurface to the deeper region of nanoindented 4H-SiC. N doping is found to weaken the bond strength of 4H-SiC, which enhances the glide and piling up of BPDs. In contrast, V doping effectively hinders the glide of BPDs, which accumulates high-stress field upon nanoindentation. The high-stress field enhances the polymorph transitions from 4H-SiC to 3C-SiC and amorphous SiC. With the insight on the effects of doping on the deformation of 4H-SiC, our work paves the way for design of the processing for differently doped 4H-SiC substrate wafers.

Undoped, V-doped, and N-doped 4H-SiC substrate wafers were purchased from SICC Co., Ltd. In V-doped and N-doped 4H-SiC substrate wafers, the concentrations of V and N are found to on the order of magnitude of 10^{17} and 10^{19} cm^{-3}, respectively (Fig. S1). The surface roughnesses of the Si face for all the substrate wafers are all smaller than 0.2 nm. Nanoindentation tests were conducted using a nanoindentation system (Nanointender G200, Agilent) with a Berkovich indenter. Various peak loads ranging from 50 to 500 mN were carried out on the Si face of all the substrate wafers. The indents for each load were repeated for eight times to obtain reliable data. During each nanoindentation test, the loading time and unloading time were both 10 s, and the holding time was 5 s. The indenter ridge was set to be parallel to the [1$\bar{1}$00] of the 4H-SiC substrate wafer, as shown in Fig. S2. Confocal Raman spectroscopy was carried out using a WITec Alpha300R micro-Raman spectrometer with a 75 mW green-diode laser operating at 532 nm. A scanning electron microscope (SEM) (Carlzeiss, Gemini300) was employed to characterize the lengths of cracks for nanoindented 4H-SiC. The cross-sectional transmission electron microscopy (TEM) specimens of the indents were prepared using a focused ion beam (FEI, Helios 5 UX). TEM and high-resolution TEM (HRTEM) micrographs were obtained by a FEI Tecnai G^2 TEM operated with the accelerating voltage of 300 kV.

The load–displacement curves of 4H-SiC substrate wafers under peak loads (P_{max}) ranging from 50 to 500 mN are smooth. As shown in the inset of Fig. 1(a), the only pop-in event occurs at the load of 400 mN in undoped 4H-SiC. Because the pop-in behavior occurs under relatively large load, the pop-in event is most likely to associate with the formation and propagation of cracks in undoped 4H-SiC. As shown in Fig. S2, the maximum indentation depths for undoped, V-doped, and N-doped 4H-SiC under the peak load are 500 mN are 994, 990, and 1015 nm, respectively. The measured elastic modulus and hardness of 4H-SiC as functions of the indentation load are plotted in Fig. 1. The hardness of 4H-SiC decreases with the increase of indentation load, as a result of the indentation size effect (ISE).[17] In the non-ISE region, the hardness of undoped 4H-SiC is 34.8 ± 0.4 GPa, which is consistent with those reported in the literature.[18] More significantly, we find that the hardness of 4H-SiC decreases on the order of V doping, undoping, and N doping, which coincides well with the dopant dependence of the penetration depths. This explains why the N-doped 4H-SiC boules are easier to be sliced, and the slicing-induced damage is easier to be removed by the following lapping.[19]
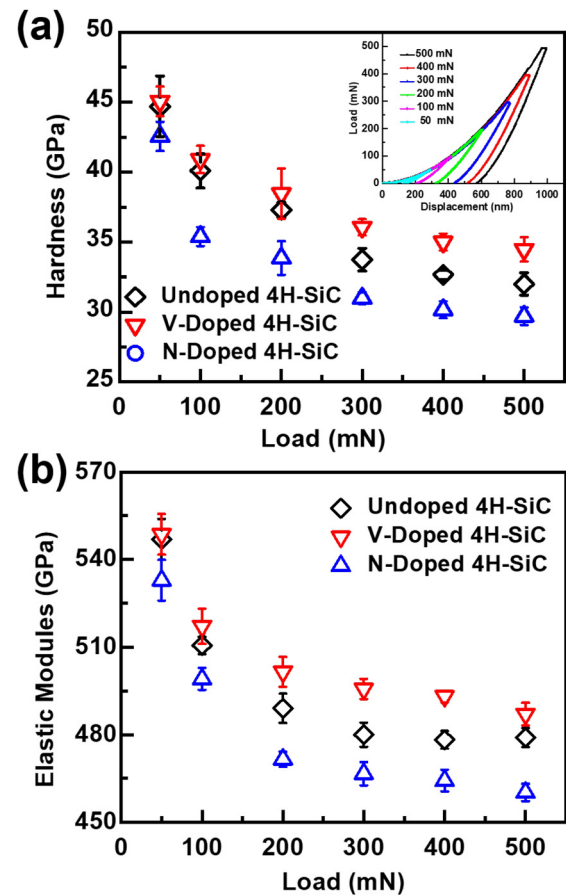

FIG. 1. The average values of (a) hardness and (b) elastic modulus as functions of the indentation depth for undoped 4H-SiC, V-doped 4H-SiC, and N-doped 4H-SiC. The indents on each wafer were repeated for eight times with the error bars connecting the maximum and the minimum values.

The hardness of semiconductors is related to the glide and piling up of dislocations.[20,21] For 4H-SiC, the dominant dislocation responsible for the deformation is the BPD. One of the most important factors affecting the glide of BPDs is the stacking fault energy (SFE). The increase in SFE indicates that SFs are difficult to expand, which makes BPDs difficult to glide and easier to cross slip. Because the values of SFE for 4H-SiC decrease on the order of V doping, undoping, and N doping,[10,20] the hardness of 4H-SiC decreases on the order of V doping, undoping, and N doping.

As shown in Fig. 1(b), the elastic modulus of 4H-SiC decreases as the indentation load increases, which is ascribed to the combined effect of surface roughness, tip roundness, and tip area function.[20] When the indentation load increases to the value larger than 400 mN, the elastic modulus for undoped 4H-SiC reaches the saturation value of 479 ± 3.2 GPa, which agrees well with previous results.[21] Furthermore, we find that the elastic modulus of 4H-SiC decreases on the order of V doping, undoping, and N doping. The effect of dopants on the elastic modulus of 4H-SiC can be understood by the effect of dopants on the bond strength.[22,23] In 4H-SiC, N and V are stabilized at the substitutional sites of C and Si, respectively.[24] Upon doping,
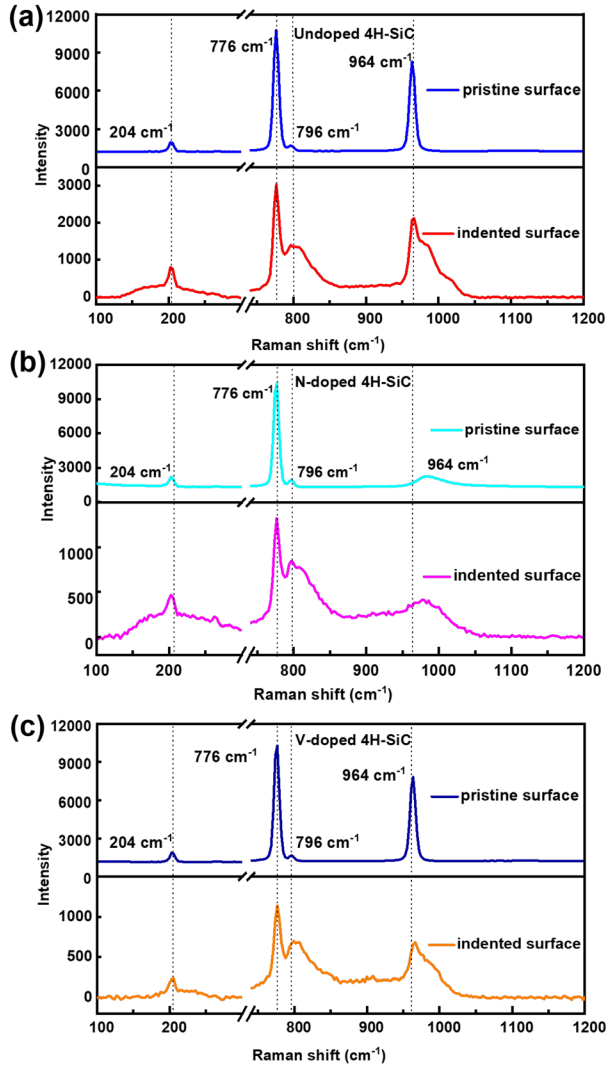
FIG. 2. Raman spectra obtained at the pristine surface and nanoindented surface for (a) undoped, (b) N-doped, and (c) V-doped 4H-SiC under the peak load of 500 mN.

V–C bonds and N–Si bonds substitute parts of original Si–C bonds in V-doped and N-doped 4H-SiC, respectively. The bond strength increases on the order of N–Si (439 KJ/mol),[25] Si–C (451 KJ/mol),[25] and V–C (469 KJ/mol).[26] Therefore, the bonds are strengthened upon V doping while weakened upon N doping, which gives rise to the enhanced elastic modulus in V-doped 4H-SiC and the reduced elastic modulus in N-doped 4H-SiC.

We then calculate the indentation fraction toughness (K_{IC}) by[27]

$$K_{IC} = A \left(\frac{a}{l} \right)^{\frac{1}{2}} \left(\frac{E}{H} \right)^{\frac{2}{3}} \frac{P}{c^{2/3}}, \tag{1}$$

where A is a constant that relates to the indenter geometry (for the Berkovich indenter used in our work, A = 0.0016), P is the applied load, c is the crack length, a is the indent size from center to corner, l is

the crack length from the indent corner to crack tip ($c = a + l$), and E and H are the elastic modulus and hardness of 4H-SiC, respectively. The crack length c of the indent is determined by

$$c = \frac{1}{3}(c_1 + c_2 + c_3). \tag{2}$$

The definition of c_1, c_2, c_3 is illustrated in Fig. S4. The values of a and l are defined by the same approach (as shown in Fig. S4). The calculated crack length, as well as the values of K_{IC} for undoped 4H-SiC, N-doped 4H-SiC, and V-doped 4H-SiC are tabulated in Table I. The crack length increases on the order of V-doping, undoping, and N-doping. Meanwhile, V doping increases the fracture toughness of 4H-SiC, while N doping decreases the fracture toughness of 4H-SiC. The changes in the fracture toughness for differently doped 4H-SiC are attributable to the changes in bonding energies.

In order to clarify the effect of dopants on the deformation mechanism of nanoindented 4H-SiC, the crystalline properties, lattice distortions, and electronic properties of the nanoindented region were investigated by micro-Raman spectroscopy. As shown in Fig. 2(a), the folded mode of the transverse acoustic branch (FTA) located at 204 cm^{-1}, the folded modes of the transverse optical branches (FTO) located at 776 and 796 cm^{-1}, as well as the folded mode of the longitudinal optical branches (FLO) located at 964 cm^{-1} are found at the pristine and nanoindented surface of 4H-SiC, which agree well with previous research.[28,29] We first discuss the effect of nanoindentation on the structural properties of 4H-SiC. As shown in Fig. 2, the intensities of the FTA peak, FLO peak, and FTO peak all decrease after nanoindentation as a result of atomic displacement during nanoindentation. Because the broadening of the FTA peak only relates to the crystalline character of 4H-SiC,[28] we compare the broadening of the FTA peaks to evaluate the effect of nanoindentation on the structural change of differently doped 4H-SiC. The broadening of the FTA peak for nanoindented 4H-SiC increases on the order of V doping, undoping, and N doping, indicating that the hardness and fracture toughness of 4H-SiC decrease on the order of V doping, undoping, and N doping, which verifies the mechanical properties of 4H-SiC measured by nanoindentation. The change in the intensity of the FTO (796 cm^{-1}) may be attributed to either a phase transition or a severe lattice distortion.[26] To distinguish these possibilities, we take the intensity of the FTA mode into account. The relative variation of these two peaks can be used to characterize the phase transition of 4H-SiC.[28] Therefore, we take the intensity ratio for the FTO peak to FTA peak as $r\left(\frac{FTO}{FTA}\right)$ to characterize the phase transition of nanoindented 4H-SiC.[28] As tabulated in Table II, the value of $r\left(\frac{FTO}{FTA}\right)$ increases after nanoindentation for all the three types of 4H-SiC, which indicates that amorphization or the polymorph transition may occur during the nanoindentation.[30]

Moreover, we find a new peak located at 972 cm^{-1}, which is attributed to the FLO mode of 3C-SiC.[28] For V-doped 4H-SiC, we find that the peak of the FTA mode is broader than that of undoped 4H-SiC as a result of the lattice distortion caused by the large size mismatch between V and Si. After nanoindentation, the increase in $r\left(\frac{FTO}{FTA}\right)$ for V-doped 4H-SiC is more prominent than that of undoped 4H-SiC. This indicates that the amorphization or the polymorph transition for nanoindented V-doped 4H-SiC is more prominent than that of nanoindented undoped 4H-SiC. For N-doped 4H-SiC, the peak of the FLO mode notably shifts to higher wavenumbers as a result of

TABLE I. Crack lengths (c), indentation fracture toughness (K_{IC}) for undoped, V-doped, and N-doped 4H-SiC.

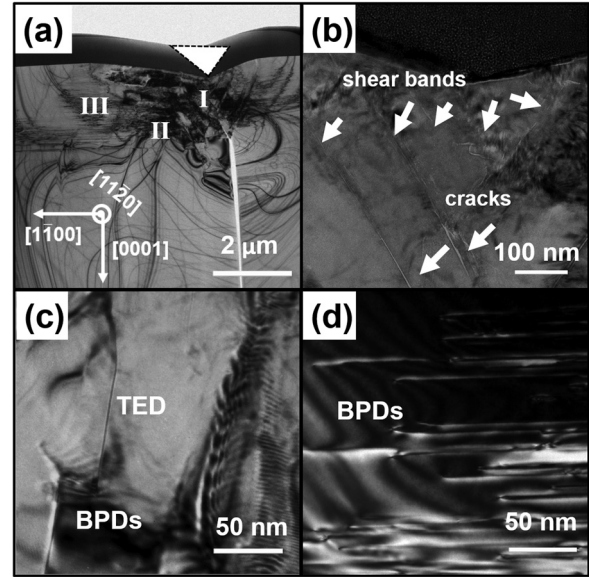|	Undoped 4H-SiC	N-doped 4H-SiC	V-doped 4H-SiC
Crack length (μm)	6.66 ± 0.34	7.36 ± 0.36	6.00 ± 0.44
K_{IC} (MPa m$^{1/2}$)	2.35 ± 0.01	1.74 ± 0.01	2.37 ± 0.02

increasing electron concentration in N-doped 4H-SiC. The high concentration of N also results in the lattice distortion, which broadens the peak of the FTA mode in highly N-doped 4H-SiC. The increase in the $r\left(\frac{FTO}{FTA}\right)$ is smaller than that of V-doped 4H-SiC but slightly larger than that of undoped 4H-SiC. This indicates that the nanoindentation induced amorphization or polymorph transition increases on the order of undoped 4H-SiC, N-doped 4H-SiC, and V-doped 4H-SiC. In N-doped 4H-SiC, the nanoindentation-induced stress can be easily released by the slip of BPDs. In V-doped 4H-SiC, where BPDs are more difficult to slip due to the higher SFE, the nanoindentation-induced stress is more difficult to be released by the slip of BPD. The high stress field, thus, enhances the polymorph transition from 4H-SiC to amorphous SiC and 3C-SiC.

We then take V-doped 4H-SiC as an example to observe the indent by TEM to clarify the microstructure of the nanoindented 4H-SiC. As shown in Fig. 3(a), the piling up of dislocations is found at the subsurface of the indent, which is found to be the origin of the decrease of the intensities of the FTA, FLO, and FTO peaks for nano-indented 4H-SiC. Below the deformation region, a long median crack extends straightly downwards the interior 4H-SiC as a result of brittle deformation.[31] According to the density of dislocations, we divide the deformation region into three regions, which are referred to as region I, region II, and region III. As shown in Fig. 3(b), region I is severely deformed, which is featured by high density of shear bands beneath the nanoindented surface. Region II is characterized by the formation of Moiré fringes, which originate from the rotation superposition of two neighboring lattices with the same spacing. BPDs connected by a TED are observed around the Moiré fringes [Fig. 3(c)]. As shown in Fig. 3(d), region III is characterized by the formation of high density of BPDs.

HRTEM observations on the severally deformed region I are then carried out to observe the detailed structural deformation of nanoindented 4H-SiC. As shown in Fig. 4(b), amorphization is

TABLE II. Summary of the Raman intensities for the FTO mode (796 cm^{-1}), FTA mode (204 cm^{-1}), and their ratio $r\left(\frac{FTO}{FTA}\right)$ at the pristine surface, as well as those at the nanoindented surface for undoped, V-doped, and N-doped 4H-SiC.

		796 cm^{-1}	204 cm^{-1}	$r\left(\frac{FTO}{FTA}\right)$
Undoped 4H-SiC	Pristine surface	1712	1952	0.88
	Indented surface	1396	802	1.74
V-doped 4H-SiC	Pristine surface	1672	1875	0.89
	Indented surface	696	234	2.97
N-doped 4H-SiC	Pristine surface	1925	2183	0.88
	Indented surface	843	463.8	1.82

FIG. 3. (a) Cross-sectional TEM image of an indent imprint in V-doped 4H-SiC. The indenter is indicated by the white triangle. (b)–(d) Zoom-in images for regions I–III as displayed in (a).

found in the subsurface of the indent. The fast Fourier transform (FFT) image of the area verifies the existence of the amorphous layer. For the deeper region away from the indent, the staking sequence of atomic layers transforms to that of 3C-SiC [Fig. 4(c)]. The FFT image of the region consistently indexed as that of the $\langle 110 \rangle$ diffraction of 3C-SiC. TEM and HRTEM observations give direct evidence for the deformation mechanism of the nanoindented 4H-SiC. BPDs, TEDs, and cracks are formed during the nanoindentation. Microscopically, the phase transitions from 4H-SiC to amorphous SiC and 3C-SiC are found as the penetration depth of the indent increases from the subsurface to the deeper region of 4H-SiC.

We also carried out TEM and HRTEM observations on the indent imprints of undoped and N-doped 4H-SiC. As shown in Fig. S5, BPDs, TEDs, and cracks are also formed after the nanoindentation of undoped and N-doped 4H-SiC. By comparing the cross-sectional TEM images for the indent imprints of differently doped 4H-SiC, we find that the density of BPDs is the largest in N-doped 4H-SiC, which coincides well with the Raman results. There are two cracks appearing near the shear bands, which indicates that N doping lowers the fracture toughness of 4H-SiC. The density of BPDs is the lowest in nano-indented V-doped 4H-SiC, while the phase transition is only observed in nanoindented V-doped 4H-SiC, which indicates that V doping hinders the formation and slip of BPDs, accumulating high-stress field upon nanoindentation. The high-stress field enhances the polymorph transitions from 4H-SiC to amorphous SiC and 3C-SiC.

It should be noted that in semi-insulating (undoped and V-doped) and n-type (N-doped) 4H-SiC substrate wafers, the dominant intrinsic defect is the carbon vacancy (V_C). It was found the concentration of V_C is on the order of magnitude of 10^{12}–10^{15} cm^{-3}.[32,33] The concentrations for common impurities of oxygen and hydrogen are found to be on the order of magnitude of 10^{12} and 10^{14} cm^{-3}, respectively.[34,35] The concentrations of V_C and common impurities are
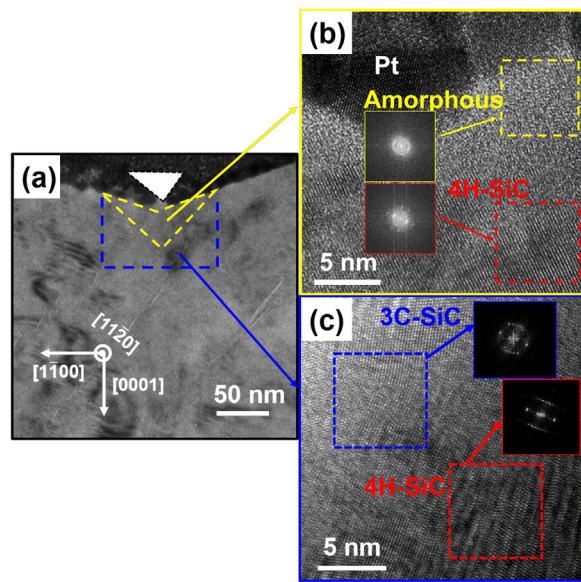
FIG. 4. (a) Cross-sectional TEM image of an indent imprint. The indenter is indicated by the white triangle. (b) and (c) HRTEM images of the region marked by the dotted lines in (a). Phase transition from 4H-SiC to amorphous SiC and 3C-SiC are found as the penetration depth of the indent increases from the subsurface to the deeper region of V-doped 4H-SiC.

negligible compared to those of N ($\sim 10^{19}$ cm^{-3}) and V ($\sim 10^{17}$ cm^{-3}). Therefore, the effect of dopants significantly prevails over the effect of intrinsic defects and common impurities on the deformation and mechanical properties of 4H-SiC.

Finally, we discuss the role of dopants on the processing of 4H-SiC substrate wafers. The hardness and fracture toughness of 4H-SiC increase in the order to N doping, undoping, and V doping. During the processing of differently doped 4H-SiC substrate wafers, the flatness-control difficulty increases in the order to V doping, undoping, and N doping. With the same processing parameters, the processing damage and removal rate of 4H-SiC substrate wafers increase in the order to V doping, undoping, and N doping. Therefore, less processing loss is expected for V-doped 4H-SiC substrate wafers.

In conclusion, we have systematically investigated the deformation mechanism and mechanical properties of N-doped, V-doped, and undoped 4H-SiC by using nanoindentation. It has been found that the mechanical properties, including the hardness, elastic modulus, and fracture toughness of 4H-SiC all decrease on the order of V doping, undoping, and N doping. During the nanoindentation, BPDs, TEDs, and cracks are formed due to the shear stress in all the three types of 4H-SiC. Polymorph transitions from 4H-SiC to 3C-SiC and amorphous SiC have been found as the penetration depth of the indent increases from the subsurface to the deeper region of 4H-SiC. The dopant-dependence for the deformation of 4H-SiC has been established. N doping is found to weaken the bond strength of 4H-SiC, enhancing the slip and piling up of BPDs. In contrast, V doping effectively hinders the slip of BPDs, accumulating high-stress field upon indentation. The high-stress field enhances the polymorph transitions from 4H-SiC to amorphous SiC and 3C-SiC. With the insight on the effects of doping on the deformation of 4H-SiC, our work paves the way for design of the processing for differently doped 4H-SiC wafers.

See the supplementary material for details on sample preparation and discussion of the typical load–displacement curves of 4H-SiC, TEM, and HRTEM images of nanoindented undoped 4H-SiC and N-doped 4H-SiC, as well as details on fracture toughness calculations.

AUTHOR DECLARATIONS
Conflict of Interest

The authors have no conflicts to disclose.

DATA AVAILABILITY

The data that support the findings of this study are available from the corresponding authors upon reasonable request.

REFERENCES

[1]T. Kimoto and J. A. Cooper, *Fundamentals of Silicon Carbide Technology: Growth, Characterization, Devices and Applications* (Wiley, 2014).
[2]E. Aradi, J. Lewis-Fell, G. Greaves, S. E. Donnelly, and J. A. Hinks, Acta Mater. **210**, 116820 (2021).
[3]S. Yang, Y. Nakagawa, M. Kondo, and T. Shibayama, Acta Mater. **211**, 116845 (2021).
[4]D. M. Lukin, C. Dory, M. A. Guidry, K. Y. Yang, S. D. Mishra, R. Trivedi, M. Radulaski, S. Sun, D. Vercruysse, G. H. Ahn, and J. Vuckovic, Nat. Photonics **14**, 330–334 (2020).
[5]Z. Tian, X. Xu, F. Jiang, J. Lu, and Q. Luo, and J. Lin, Ceram. Int. **45**, 21998 (2019).
[6]S.-I. Nakashima, T. Mitani, M. Tomobe, T. Kato, and H. Okumura, AIP Adv. **6**, 015207 (2016).
[7]H. Yashiro, T. Fujimoto, N. Ohtani, T. Hoshino, M. Katsuno, T. Aigo, H. Tsuge, M. Nakabayashi, H. Hirano, and K. Tatsumi, Mater. Sci. Forum **600**, 819–822 (2008).
[8]S. Goel, J. Yan, X. Luo, and A. Agrawal, J. Mech. Behav. Biomed. Mater. **34**, 330–337 (2014).
[9]A. Nawaz, W. G. Mao, C. Lu, and Y. G. Shen, J. Mech. Behav. Biomed. Mater. **66**, 172–180 (2017).
[10]B. Zhu, D. Zhao, and H. Zhao, Ceram. Int. **45**, 5150–5157 (2019).
[11]H. J. Chung, J. Q. Liu, and M. Skowronski, Appl. Phys. Lett. **81**, 3759–3761 (2002).
[12]S. Kultayeva, Y.-W. Kim, and I.-H. Song, J. Eur. Ceram. **41**, 4006–4015 (2021).
[13]Y. Cui, X. Hu, K. Yang, X. Yang, X. Xie, L. Xiao, and X. Xu, Cryst. Growth Des. **15**, 3131–3136 (2015).
[14]M. K. Linnarsson, A. Hallen, and L. Vines, Semicond. Sci. Technol. **34**, 115006 (2019).
[15]F. Fujie, S. Harada, K. Hanada, H. Suo, H. Koizumi, T. Kato, M. Tagewa, and T. Ujihara, Acta Mater. **194**, 387 (2020).
[16]V. I. Orlov, G. Regula, and E. B. Yakimov, Acta Mater. **139**, 155 (2017).
[17]T. F. Page, L. Riester, and S. V. Hainsworth, MRS Proc. **522**, 113–118 (1998).
[18]M. Matsumoto, H. Huang, H. Harada, K. Kakimoto, and J. Yan, J. Phys. D **50**, 265303 (2017).
[19]J. Lu, Q. Luo, X. Xu, H. Huang, and F. Jiang, Proc. Inst. Mech. Eng. B J. Eng. Manuf. **233**, 69–76 (2017).
[20]I. Yonenaga, Physica B **308–310**, 1150–1152 (2001).

[21] X. J. Ning, N. Huvey, and P. Pirouz, J. Am. Ceram. Soc. **80**, 1645–1652 (2005).

[22] L. Chen, A. Ahadi, J. Zhou, and J.-E. Ståhl, Procedia CIRP **8**, 334–339 (2013).

[23] L. Pizzagalli, Acta Mater. **78**, 236–244 (2014).

[24] W. C. Mitchel, R. Perrin, J. Goldstein, A. Saxler, M. Roth, S. R. Smith, J. S. Solomon, and A. O. Evwaraye, J. Appl. Phys. **86**, 5040–5044 (1999).

[25] J. Drowart, G. Demaria, and M. G. Inghram, J. Chem. Phys. **29**, 1015–1021 (1958).

[26] R. Weast, *CRC Handbook of Chemistry and Physics* (CRC Press, 1988).

[27] K. I. Schiffmann, Philos. Mag. Lett. **91**, 1163–1178 (2011).

[28] S. Nakashima and H. Harima, Phys. Status Solidi A **162**, 39–64 (1997).

[29] J. Yang, H. Song, J. Jian, W. Wang, and X. Chen, J. Cryst. Growth **568**, 126182 (2021).

[30] N. A. Mahadik, R. E. Stahlbush, S. B. Qadri, O. J. Glembocki, D. A. Alexson, K. D. Hobart, J. D. Caldwell, R. L. Myers-Ward, J. L. Tedesco, C. R. Eddy, and D. Gaskill, J. Electron. Mater. **40**, 413–418 (2011).

[31] B. Lawn and R. Wilshaw, "Indentation fracture: Principles and applications," J. Mater. Sci. **10**, 1049–1081 (1975).

[32] B. Zippeliusa, J. Sudab, and T. Kimotoc, J. Appl. Phys. **111**, 033515 (2012).

[33] T. Miyazawaa and H. Tsuchida, J. Appl. Phys. **113**, 083714 (2013).

[34] K. Yamashita, M. Kitabatake, P. Kusumoto, K. Takahashi, M. Uchida, R. Miyanaga, H. Itoh, and M. Yoshikawa, Mater. Sci. Forum **389**, 1037 (2002).

[35] M. K. Linnarsson, U. Forsberg, M. S. Janson, E. Janzen, and B. G. Svensson, Mater. Sci. Forum **389**, 565 (2002).